Electrically driven nuclear spin resonance in single-molecule magnets

Stefan Thiele *et al.*

Science **344**, 1135 (2014);
DOI: 10.1126/science.1249802

Science (print ISSN 0036-8075; online ISSN 1095-9203) is published weekly, except the last week in December, by the American Association for the Advancement of Science, 1200 New York Avenue NW, Washington, DC 20005.

QUANTUM INFORMATION

Electrically driven nuclear spin resonance in single-molecule magnets

Stefan Thiele,[1,2] Franck Balestro,[1,2,3] Rafik Ballou,[1,2] Svetlana Klyatskaya,[4] Mario Ruben,[4,5] Wolfgang Wernsdorfer[1,2]*

Recent advances in addressing isolated nuclear spins have opened up a path toward using nuclear-spin–based quantum bits. Local magnetic fields are normally used to coherently manipulate the state of the nuclear spin; however, electrical manipulation would allow for fast switching and spatially confined spin control. Here, we propose and demonstrate coherent single nuclear spin manipulation using electric fields only. Because there is no direct coupling between the spin and the electric field, we make use of the hyperfine Stark effect as a magnetic field transducer at the atomic level. This quantum-mechanical process is present in all nuclear spin systems, such as phosphorus or bismuth atoms in silicon, and offers a general route toward the electrical control of nuclear-spin–based devices.

The realization of a functional quantum computer is currently one of the most ambitious technological goals. Among existing concepts (*1*–*3*), devices in which the quantum bits (qubits) are encoded by spins are very attractive, as they benefit from the steady progress in nanofabrication and allow for electrical readout of the qubit states (*4*–*6*). Nuclear-spin–based devices are better isolated from the environment than their electron spin counterparts (*7*), but their detection and manipulation remain challenging.

Operating nuclear spin qubits have been demonstrated with devices based on nitrogen vacancy centers (*8*), single-molecule magnets (*9*–*11*), and silicon (*12*). Yet, their integration remains limited by the on-chip microcoils (*13*) used to manipulate the spin. The parasitic crosstalk to neighboring spin qubits and the large currents necessary to perform quantum operations are serious limiting factors. Using electric fields instead of magnetic fields to manipulate the spin would alleviate this problem, as only small displacement currents are required; in addition, electric fields can be easily focused and shielded within a small volume. The coupling of the spin to the electric field is established by the hyperfine Stark effect, which transforms the electric field into a local magnetic field. Moreover, the static hyperfine Stark effect can be used

[1]CNRS, Inst NEEL, F-38042 Grenoble, France. [2]Université Grenoble Alpes, Inst NEEL, F-38042 Grenoble, France. [3]Institut Universitaire de France, 103 boulevard Saint-Michel, 75005 Paris, France. [4]Institute of Nanotechnology, Karlsruhe Institute of Technology, 76344 Eggenstein-Leopoldshafen, Germany. [5]Institut de Physique et de Chimie des Materiaux de Strasbourg, CNRS, 67034 Strasbourg, France.
*Corresponding author. E-mail: wolfgang.wernsdorfer@neel.cnrs.fr

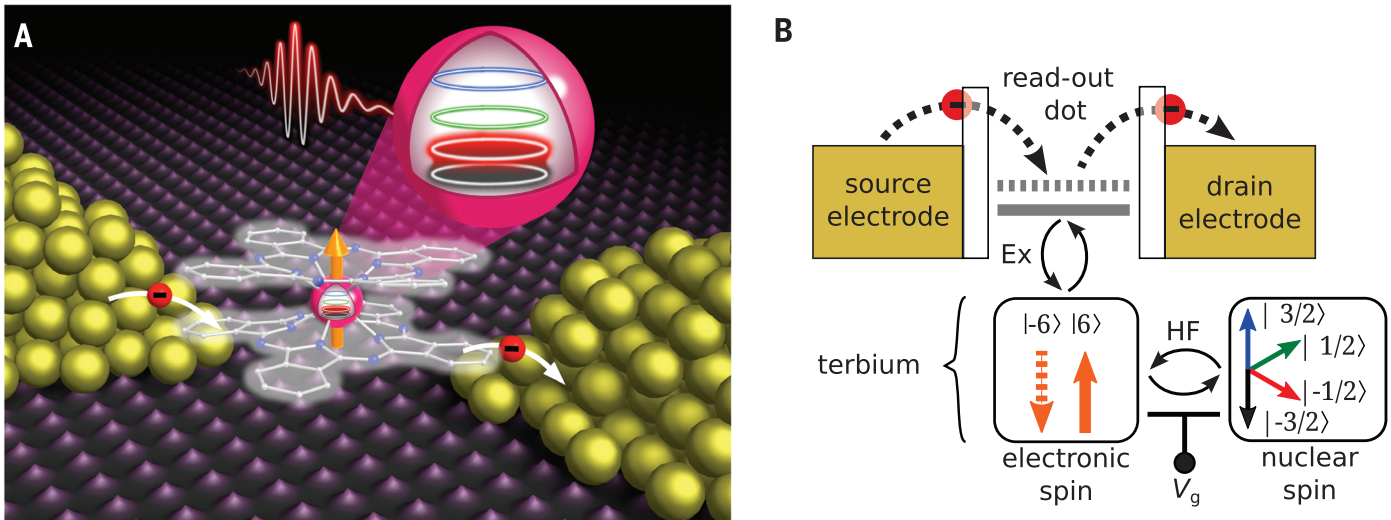

Fig. 1. Nuclear spin qubit transistor and its detection scheme. (**A**) Artist's view of a nuclear spin qubit transistor based on a single $TbPc_2$ molecular magnet. The molecule, consisting of a Tb^{3+} ion (pink) sandwiched between two Pc-ligands (white), is coupled to source, drain, and gate (not shown) electrodes. The four anisotropic nuclear spin states of the Tb^{3+} (colored circles) can be manipulated with an electric field pulse. (**B**) Three coupled subsystems of the transistor: (i) The four-level nuclear spin qubit is hyperfine (HF) coupled to (ii) an Ising-like electronic spin, which in turn is antiferromagnetically exchange (Ex) coupled to (iii) a readout quantum dot.

to tune individual nuclear qubits in and out of resonance (*14*) and thus allows for the individual addressability of different nuclear spin qubits.

To perform our experiments, we used a three-terminal nuclear spin qubit transistor (*9*) (Fig. 1A). We studied the transistor, consisting of a $TbPc_2$ single-molecule magnet coupled to source, drain, and gate electrodes, by performing electrical transport measurements inside a dilution refrigerator at 40 mK. We can associate the device with three coupled quantum systems (Fig. 1B):

(i) A nuclear spin qubit emerging from the atomic core of the Tb^{3+} ion. It possesses a nuclear spin $I = 3/2$ leading to four different qubit states: $|-3/2\rangle, |-1/2\rangle, |+1/2\rangle$, and $|+3/2\rangle$.

(ii) An electronic spin arising from the 4f electrons of the terbium. Its electronic configuration is $[Xe]4f^8$ resulting in a total spin of $S = 3$ and a total orbital momentum of $L = 3$. A strong spin-orbit coupling yields an electronic spin with a total angular magnetic moment of $J = 6$. In addition, the ligand field, generated by the two Pc's, leads to a well-isolated electron spin ground state doublet of $|\uparrow\rangle$ and $|\downarrow\rangle$ with a uniaxial anisotropy axis perpendicular to the Pc plane. The degeneracy of the doublet is lifted by the hyperfine coupling to the nuclear spin qubit and splits each electronic spin ground state into four different quantum states. At zero external field, the energy levels are intrinsically separated by $\nu_{01} \approx 2.(5)$ GHz, $\nu_{12} \approx 3.(1)$ GHz, and $\nu_{23} \approx 3.(7)$ GHz, where the index 0 corresponds to the ground state, and indices 1, 2, and 3 to the first, second, and third excited states, respectively (Fig. 2A).

(iii) A readout quantum dot created by the Pc ligands. Their delocalized π-electron system is tunnel-coupled to the source and drain terminals, creating a quantum dot in the vicinity of the electronic spin carried by the Tb^{3+} ion. Furthermore, an overlap of the delocalized π-electron system with the terbium's 4f wave functions gives rise to an exchange coupling of $E_{ex} \approx 1.66$ T between the readout quantum dot and the electronic spin (*15*).

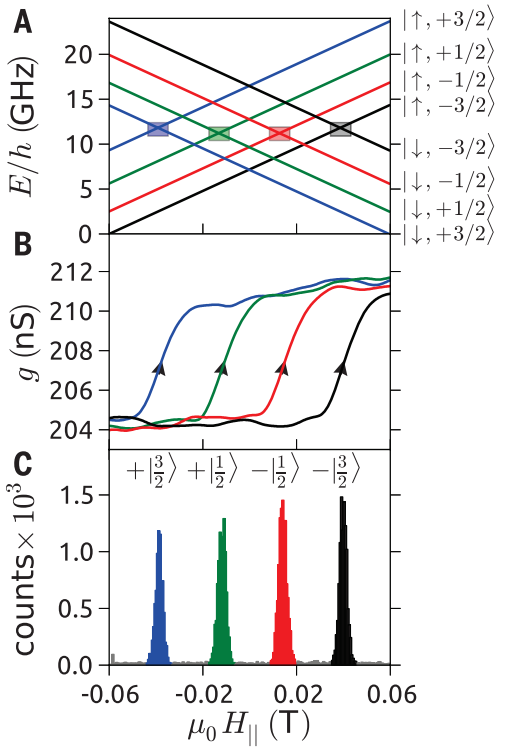

Fig. 2. Zeeman diagram and nuclear spin detection procedure. (**A**) Zeeman diagram of the $TbPc_2$ molecular magnet, showing the hyperfine split electronic spin ground state doublet $|\uparrow\rangle$ and $|\downarrow\rangle$ as a function of the external magnetic field $H_{||}$ parallel to the easy-axis of magnetization. The ligand-field–induced avoided level crossings (colored rectangles) allow for tunneling of the electron spin. (**B**) The jumps of the conductance g of the readout quantum dot during magnetic-field sweeps are nuclear-spin dependent. (**C**) Histograms of the positions of about 75,000 conductance jumps, showing four nonoverlapping Gaussian-like distributions; each conductance jump can be assigned to a nuclear spin state.

To perform the readout of the single-nuclear spin state, we exploit the different interactions between the three quantum systems.

First, the hyperfine interaction splits each electronic ground state doublet into four nuclear-spin–dependent levels (Fig. 2A). Electronic levels corresponding to the same nuclear spin state are mixed owing to the off-diagonal terms in the ligand-field Hamiltonian; in an external magnetic field, this results in avoided level crossings of $\Delta E \approx 1\ \mu K$ (rectangles in Fig. 2A). Sweeping the magnetic field slowly enough over such an anti-crossing gives rise to the quantum tunneling of magnetization (QTM) (*16*, *17*), which reverses the electronic spin according to the Landau-Zener probability (*18*, *19*). Because the magnetic field position of the QTM is nuclear spin dependent, we can use this process to measure the state of the nuclear spin qubit (*9*–*11*).

In the second stage, the electronic spin is mapped onto the readout dot's conductance through use of the exchange interaction (*15*). It

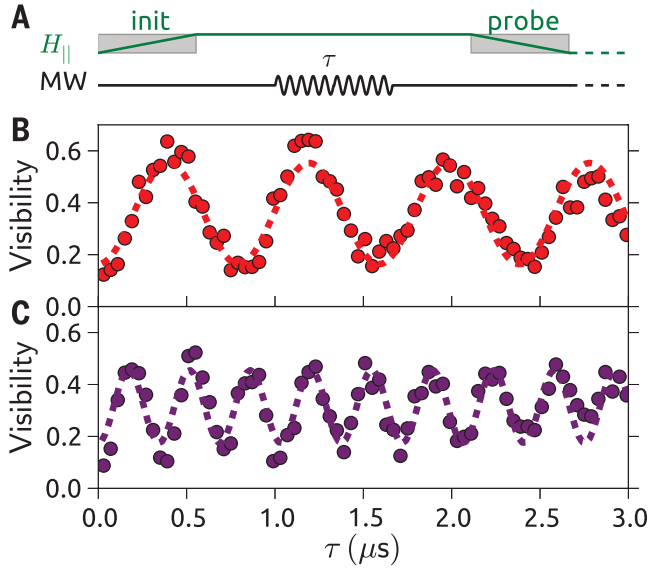

Fig. 3. Rabi oscillations of a single nuclear spin qubit. (**A**) Time-dependent external magnetic field $H_{||}$ and pulse sequence. The nuclear spin is first initialized in the lower $|3/2\rangle$ state (init sequence). A subsequent MW pulse of frequency ν_0 and duration τ induces an effective oscillating magnetic field resulting in coherent manipulation of the two lower states of the nuclear spin qubit. Finally, $H_{||}$ is swept back to probe the final state of the nuclear spin qubit. (**B** and **C**) Rabi oscillations between $|3/2\rangle$ and $|1/2\rangle$ states obtained by repeating the above sequence 100 times at each τ, for two different MW powers, (**B**) P_{MW} = 1 mW and (**C**) P_{MW} = 1.58 mW.

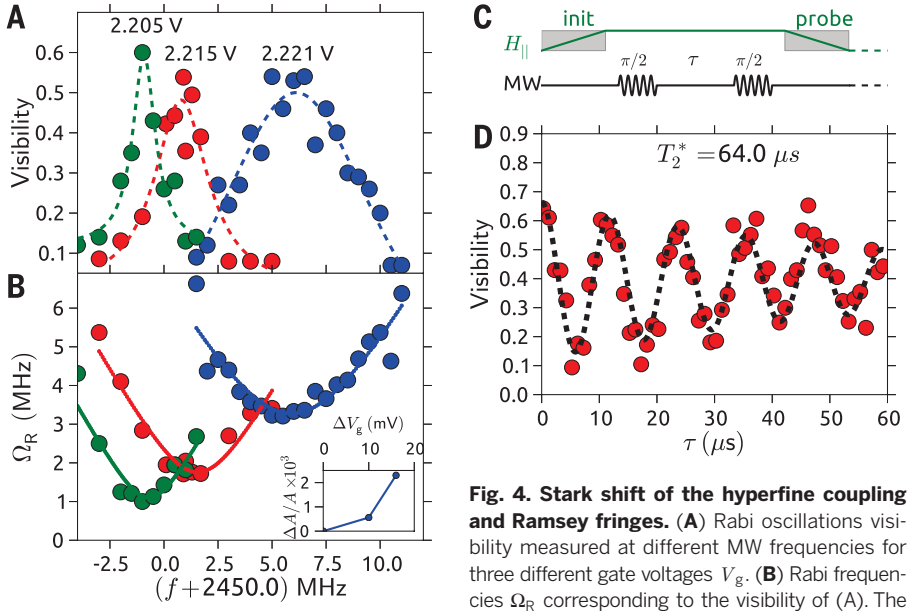

Fig. 4. Stark shift of the hyperfine coupling and Ramsey fringes. (**A**) Rabi oscillations visibility measured at different MW frequencies for three different gate voltages V_g. (**B**) Rabi frequencies Ω_R corresponding to the visibility of (A). The continuous lines are fit to the experimental points following the theoretical expression of the Rabi frequency dependence (see text). (Inset) The relative change $\Delta A/A$ with respect to the applied V_g. (**C**) Time-dependent external magnetic field $H_{||}$ and pulse sequence. Initialization and probe of the nuclear spin qubit are performed by using the identical protocol as in Fig. 3A. The MW sequence consists of two $\pi/2$ pulses, with an increasing interpulse delay τ. (**D**) Ramsey interference fringes obtained by repeating the procedure of (C) 100 times. V_g = 2.205 V, corresponding to a Rabi frequency Ω_R = 1.136 MHz and a resonant frequency ν_0 = 2.449 MHz of the nuclear spin qubit. The measured coherence time $T_2^* \approx 64$ μs.

induces a slight modification of the readout quantum dot's chemical potential depending on whether the electronic spin is $|\uparrow\rangle$ or $|\downarrow\rangle$. Therefore, when sweeping the magnetic field at constant bias and gate voltages, the reversal of the electronic spin results in a conductance jump (Fig. 2B). The amplitude of the jump is typically about 3% and its position in the magnetic field is nuclear spin state dependent.

For statistical analysis, we swept the magnetic field back and forth 75,000 times while monitoring the conductance of the readout quantum dot. By plotting the magnetic field position of all the detected conductance jumps into a histogram, we obtained four nonoverlapping peaks (Fig. 2C), which enabled us to unambiguously assign a nuclear qubit state to each detected jump. The error induced by our nuclear spin readout procedure is mainly due to inelastic electronic spin reversals, which were misinterpreted as a QTM event, and is estimated to be less than 4% (*20*). For the device presented here, we found relaxation times T_1 of ≈34 s for $m_I = \pm 3/2$ and T_1's of ≈17 s for $m_I = \pm 1/2$ (*15*).

We turn now to the electrical manipulation of a single nuclear spin. The hyperfine Stark effect describes the change of the hyperfine constant A in the Hamiltonian $H_{HF} = A\mathbf{I}\cdot\mathbf{J}$ as a function of an external electric field (*21*, *22*). Writing the Hamiltonian as $H_{HF} = g_N \mu_N \mathbf{I} \cdot \mathbf{B}_{eff}(A, J)$ demonstrates how the modification of A is converted into a change of the effective magnetic field $\mathbf{B}_{eff}(A, J)$ at the center of the nucleus. Given a HF constant of A = 24.9 mK (*23*) and $J = 6$, we obtain an effective static field of 329 T. Thus, a periodic modulation of A by 1/1000 of its value is sufficient to generate local magnetic field oscillations of ±329 mT. Because the orientation of the quantization axis of the molecule with respect to the electric field is not well determined, the effective magnetic field will have components in the x and z direction. However, in terms of oscillating fields, only the component in the x direction can rotate the nuclear spin, whereas the z component induces additional decoherence. Moreover, even moderate electric field amplitudes of 1 mV/nm are sufficient to induce a controlled fine tuning of the HF constant, which is on the order of 1% (*15*).

For the experimental demonstration of the single–nuclear-spin manipulation, we focused on the nuclear qubit subspace of $|+3/2\rangle$ and $|+1/2\rangle$, whose eigenstates are separated by $\nu_{01} \approx 2.45$ GHz [the exact value is device dependent (*23*, *24*)]. We initialize the nuclear spin qubit by sweeping the external magnetic field back and forth between ±60 mT at 80 mT/s (Fig. 3A) until a QTM transition is measured at –38 mT, which is the signature of the $|+3/2\rangle$ qubit state (Fig. 2C). We then apply a microwave (MW) pulse of duration τ and a local field amplitude on the order of ≈1 mV/nm while keeping the external magnetic field constant (Fig. 3A); the pulse modulates the hyperfine constant A at the MW frequency. Finally, we detect the resulting state by sweeping back the external magnetic field on a time scale faster than the measured relaxation times of both nuclear spin states. The entire sequence is rejected when the final state is not detected because of a missing QTM transition. Repeating this procedure resulted in coherent Rabi oscillations (Fig. 3, B and C). The visibility of the Rabi oscillations as a function of the applied MW frequency (Fig. 4A) has a maximum at the resonant frequency ν_0 and decreases for increasing detuning $\Delta = |\nu - \nu_0|$. In addition, a clear dependence of the nuclear qubit resonance frequency on the gate voltage is observed in Fig. 4A. This effect can be attributed to the static HF Stark shift, owing to the additional electric field induced by the gate voltage, which shows our ability to tune the HF constant A between the electronic spin and the nuclear spin qubit. Only the z component of the effective magnetic field will modify the level splitting. Applying a static gate voltage offset of 16 mV shifts the resonant frequency of the nuclear spin qubit by $\Delta\nu_0 \approx 7$ MHz, corresponding to $\Delta A/A \approx 0.23\%$ (Fig. 4B, inset).

To extract the Stark shift–induced effective ac magnetic driving field at the nuclei, used to

coherently manipulate the nuclear spin qubit, we measured the Rabi frequency Ω_R evolution as a function of the applied MW frequency for the three different gate voltages (Fig. 4B). The horizontal shift of the minimum is again induced by the static gate voltage, whereas the vertical evolution indicates an increasing effective ac field in the x direction, which is probably caused by the nonlinearity of the HF Stark effect. The solid lines are fits to $\Omega_R = \sqrt{\Delta^2 + (\sqrt{3} g_N \mu_N B_x/\hbar)^2}$, with g_N being the nuclear g-factor [≈1.354 for Tb (*25*)], μ_N the nuclear magneton, and B_x the effective magnetic field in the x direction. The equation gives B_x = 62, 98, and 183 mT for V_g = 2.205, 2.215, and 2.221 V, respectively, up to two orders of magnitude higher than magnetic fields created by on-chip microcoils. The electric driving field is induced along the source-drain direction, and only the x component of the corresponding effective magnetic field is responsible for the nuclear spin rotation.

We turn now to the measurements of the Ramsey fringes to assess the dephasing time T_2^* of the nuclear spin qubit, which is tantamount to the average duration over which the coherence of the quantum superposition is preserved. As shown by the pulse sequence presented in Fig. 4C, the nuclear spin qubit is first initialized in the $|3/2\rangle$ state. Subsequently, two $\pi/2$ MW pulses are generated with an interpulse delay τ. Finally, the readout of the final state is probed with the same procedure as explained previously. Repeating this procedure results in the Ramsey fringes shown in Fig. 4D. The data follow an exponentially decaying cosine function revealing a coherence time $T_2^* \approx 64\ \mu s$. Detailed studies suggest that the major contribution to the decoherence was caused by charge noise, which induced magnetic field fluctuations of about 10 mT via the HF Stark effect. Therefore, we expect that more stable gate oxides would increase T_2^* by one or two orders of magnitude.

Our results show the general feasibility of establishing an all-electrical control of a single nuclear spin through use of the hyperfine Stark effect and should be transferable to other spin qubit devices with a large hyperfine interaction.

REFERENCES AND NOTES

1. C. Monroe, D. M. Meekhof, B. E. King, W. M. Itano, D. J. Wineland, *Phys. Rev. Lett.* **75**, 4714–4717 (1995).
2. A. Wallraff *et al.*, *Nature* **431**, 162–167 (2004).
3. L. DiCarlo *et al.*, *Nature* **467**, 574–578 (2010).
4. D. Loss, D. P. DiVincenzo, *Phys. Rev. A* **57**, 120–126 (1998).
5. J. M. Elzerman *et al.*, *Nature* **430**, 431–435 (2004).
6. F. H. L. Koppens *et al.*, *Nature* **442**, 766–771 (2006).
7. P. C. Maurer *et al.*, *Science* **336**, 1283–1286 (2012).
8. P. Neumann *et al.*, *Science* **329**, 542–544 (2010).
9. R. Vincent, S. Klyatskaya, M. Ruben, W. Wernsdorfer, F. Balestro, *Nature* **488**, 357–360 (2012).
10. M. Urdampilleta, S. Klyatskaya, M. Ruben, W. Wernsdorfer, *Phys. Rev. B* **87**, 195412 (2013).
11. M. Ganzhorn, S. Klyatskaya, M. Ruben, W. Wernsdorfer, *Nat. Nanotechnol.* **8**, 165–169 (2013).
12. J. J. Pla *et al.*, *Nature* **496**, 334–338 (2013).
13. T. Obata *et al.*, *Rev. Sci. Instrum.* **78**, 104704 (2007).
14. B. E. Kane, *Nature* **393**, 133–137 (1998).
15. Materials and methods are available as supplementary materials on *Science* Online.
16. J. R. Friedman, M. P. Sarachik, J. Tejada, R. Ziolo, *Phys. Rev. Lett.* **76**, 3830–3833 (1996).
17. L. Thomas *et al.*, *Nature* **383**, 145–147 (1996).
18. L. Landau, *Physics of the Soviet Union* **2**, 46 (1932).
19. C. Zener, *Proc. R Soc. Math. Phys. Eng. Sci.* **137**, 696–702 (1932).
20. S. Thiele *et al.*, *Phys. Rev. Lett.* **111**, 037203 (2013).
21. R. Haun, J. Zacharias, *Phys. Rev.* **107**, 107–109 (1957).
22. R. Rahman *et al.*, *Phys. Rev. Lett.* **99**, 036403 (2007).
23. N. Ishikawa, M. Sugita, W. Wernsdorfer, *Angew. Chem. Int. Ed.* **44**, 2931–2935 (2005).
24. C. Hutchison, E. Wong, *J. Chem. Phys.* **29**, 754 (1958).
25. J. M. Baker, J. R. Chadwick, G. Garton, J. P. Hurrell, *Proc.R. Soc. Math. Phys. Eng. Sci.* **286**, 352–365 (1965).

ACKNOWLEDGMENTS

This work was partially supported by MoQuaS FP7-ICT-2013-10, the Deutsche Forschungsgemeinschaft Programs no. SPP 1459 and TRR 88 3Met, ANR-12-JS10-007, ANR-13-BS10-0001 MolQuSpin, and European Research Council Advanced Grant MolNanoSpin no. 226558. The samples were manufactured at the NANOFAB facilities of the Neel Institute. We acknowledge E. Bonet, O. Buisson, Y. Deschanels, F. Evers, E. Eyraud, O. Gaier, M. Ganzhorn, C. Godfrin, C. Grupe, C. Hoarau, D. Lepoittevin, T. Meunier, N. Roch, C. Thirion, M. Urdampiletta, and R. Vincent.

SUPPLEMENTARY MATERIALS

www.sciencemag.org/content/344/6188/1135/suppl/DC1
Materials and Methods
Supplementary Text
Figs. S1 to S10
References (*26*–*35*)

16 December 2013; accepted 7 May 2014
10.1126/science.1249802

INTERFACIAL CHEMISTRY

Liquid flow along a solid surface reversibly alters interfacial chemistry

Dan Lis,[1]* Ellen H. G. Backus,[2] Johannes Hunger,[2] Sapun H. Parekh,[2] Mischa Bonn[2]*

In nature, aqueous solutions often move collectively along solid surfaces (for example, raindrops falling on the ground and rivers flowing through riverbeds). However, the influence of such motion on water-surface interfacial chemistry is unclear. In this work, we combine surface-specific sum frequency generation spectroscopy and microfluidics to show that at immersed calcium fluoride and fused silica surfaces, flow leads to a reversible modification of the surface charge and subsequent realignment of the interfacial water molecules. Obtaining equivalent effects under static conditions requires a substantial change in bulk solution pH (up to 2 pH units), demonstrating the coupling between flow and chemistry. These marked flow-induced variations in interfacial chemistry should substantially affect our understanding and modeling of chemical processes at immersed surfaces.

The chemistry taking place at the interface between a solid material and an aqueous solution is relevant for a variety of disciplines, including geology, environmental sciences, and catalysis (*1*–*3*). The local chemical composition at the interface strongly influences the reactivity of the system, as has been demonstrated, for example, in geological studies of weathering (*4*). Similarly, the abrasion and dissolution of materials immersed in aqueous solutions is at the heart of environmental concerns. Dissolution of ocean organisms' shells and skeletons stemming from increasing acidification of water could lead to potentially devastating consequences for marine life (*5*). Accurate knowledge of the composition of both the solid material and the aqueous solution locally at the surface is essential to understand, model, and predict these interfacial chemical processes.

Previous studies have shown that the structure of liquid water at a solid interface is different from that of the bulk phase (*6*–*8*) and can resemble the ice structure (*9*) because of the specific physico-chemical properties of the surface (e.g., charge, morphology, wetting properties). Generally speaking, interfacial water possesses a more structured hydrogen bonding network than bulk water. Among various factors, the solid surface holding a net electric charge acts to align the static dipole of water molecules at the surface (Fig. 1A, top). The length over which the electric field extends into the solution from the surface is referred to as the Debye length (*10*) and correlates with the distance from the surface that water retains its preferential alignment (~ 1 to 10 nm).

In addition to causing water alignment at the surface, the charge present at the interface also attracts ions from the solution to the interface, causing surface-charge screening and leading to the formation of the so-called electrical double layer (*10*). Accordingly, the composition, as well as the structure, of the fluid adjacent to the surface can vary substantially compared with the bulk (*11*–*14*). Molecular dynamics simulations have shown, for instance, that the interfacial pH can be quite different from the bulk (*11*). Although substantial progress regarding interfacial composition and molecular organization has been achieved, in nearly all of these studies on solid-liquid

[1]Department of Physics, University of Namur, Rue de Bruxelles 61, 5000 Namur, Belgium. [2]Department of Molecular Spectroscopy, Max Planck Institute for Polymer Research, Ackermannweg 10, 55128 Mainz, Germany.
*Corresponding author. E-mail: dan.lis@unamur.be (D.L.); bonn@mpip-mainz.mpg.de (M.B.)